

Multiphysics Model Validation of Resistojets with Concentric Tubular Heat Exchanger

Federico Romei^{*†}, Angelo Grubišić^{*}, Davide Lasagna^{*} and Dave Gibbon^{**}

^{*}University of Southampton, Southampton, SO17 1BJ, UK

^{**}Surrey Satellite Technology Ltd, Guildford, GU2 7YE, UK

[†]f.romei@soton.ac.uk

Abstract

Operation of electrothermal thrusters at extreme temperatures and power densities requires a detailed understanding of numerous highly-coupled physical processes. A high-temperature resistojets produced via metal additive manufacturing is in development at the University of Southampton. This paper describes a multiphysics model and validation from data on a high-temperature hydrogen resistojets. The investigation is broken down in two domains: the nozzle, with the influence of the vacuum chamber, and the full thruster. Compressible Navier-Stokes equations coupled with Joule heating show good agreement of the model solution with experimental data, while thrust deviates from measured data at lower Reynolds number regimes.

1. Introduction

Electrothermal propulsion systems in the context of spacecraft, consist of an electrically powered heat exchanger of some form, which increase the enthalpy of a propellant. Enthalpy is traded for kinetic energy through a gas dynamic expansion process to produce a supersonic exhaust via a converging-diverging nozzle delivering thrust. The performance of a thruster is quantified by the specific impulse (ISP), which increases proportionally to the square root of the stagnation gas temperature. By increasing the stagnation temperature, the amount of propellant required on board of the spacecraft to accomplish a specific mission decreases or more total impulse is provided for a fixed quantity of propellant, which is the goal of this research.

Surrey Satellite Technology Limited (SSTL) have employed a low power hot gas system, known as a resistojets, since 2002, which uses either butane or xenon as propellant. This system has flown on twenty spacecraft including the European GPS Galileo Testbed GIOVE-A validation satellite. This low cost and relatively low temperature resistojets significantly extends the performance of traditional cold gas propulsion systems to 42 s ISP. A collaborative development program between the University of Southampton and SSTL is currently enabling a High Temperature Resistojets (HTR), targeting an ISP of 100 s. At the current time, a primary driver of resistojets technology is a requirement for the all-electric propulsion spacecraft bus. Geostationary telecommunication satellites typically use chemical propulsion for attitude control as well as orbit-raising and station-keeping. The benefit of using a xenon propellant HTR is in fuel mass savings, cost savings in launch vehicles for lighter spacecraft and further reduction of costs by eliminating the use of hazardous propellants. A second driver of the technology is the small Low Earth Orbit (LEO) platform. These satellites have limited resources, such as low volume and power budgets, therefore, they depend upon high density ISP (propellant storage density – ISP product), and rely on inert propellants to lower Assembly Integration and Testing (AIT) costs. The resulting propulsion system has low ISP, low total impulse and therefore limited on-orbit/deorbit capability. A low power and high performance HTR would meet both of these application requirements.

A validated multiphysics model is essential in this respect for both research and optimization into the thruster design and for understanding the multiphysics nature of the resistojets. The objective of the present paper is to show the results of a fully coupled multiphysics model of a high-temperature hydrogen resistojets with a concentric recirculating tubular heat exchanger. The components involved are metal parts of the heat exchanger, including a converging-diverging conical nozzle, ceramic isolators, thin foil radiation shielding and micro fibrous ceramic thermal insulation. The multiphysics model couples conductive and radiative heat transfer within the solid parts and convective heat transfer in the propellant gas, resistive dissipative heating within the heat exchanger element, and compressible Navier-Stokes (N-S) equations for the propellant gas. Model outputs include performance parameters such as thrust and heat exchanger pressure drop, as well as the full electrothermal and fluidic solution. The thermal solution of the resistojets is used to evaluate the overall efficiency of the thruster, which accounts for radiation-to-ambient, frozen flow losses, under expansion and divergence losses. A comprehensive sensitivity analysis of the computational thrust with respect to both nozzle geometric parameters and of selected thermodynamic parameters determines an error band of the numerical solution, which is compared with experimental data from the literature.

1.1. High Temperature by Selective Laser Melting Development

A next generation high temperature xenon resistojet delivering specific impulse above 80 s would be of significant benefit to both small and newer all-electric spacecraft, but would require a propellant temperature of greater than 3 000 K assuming gas dynamics expansion. At the University of Southampton, development of a novel high-temperature resistojet (HTR) concept is currently ongoing. Metal additive manufacturing, and in particular selective laser melting, has been used to produce an innovative monolithic concentric tubular heat exchanger with integrated nozzle, which has the double functionality of enabling flow recirculation and electrical heating. The maximum gas temperature is very close the maximum structural temperature of the thruster, since the heat exchanger directly heats the propellant throughout the flow path. Figure 1 show the High Temperature Resistojet schematics (left) and its prototype assembly manufactured in stainless steel to perform functional tests at the University of Southampton's David Fear Vacuum Facility. The current research is progressing towards manufacturing the HTR design using high melting point materials, such as refractory metals. A similar multiphysics model to that one shown in this paper will be applied to the HTR in order to converge not only on a workable design, but to an optimized design for SLM production.

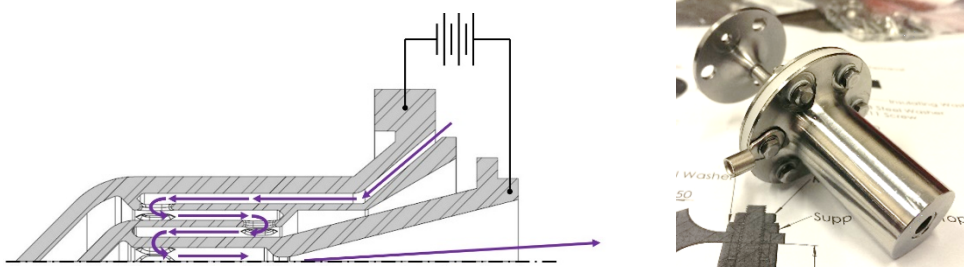


Figure 1: Axial-symmetric section view of the HTR heat exchanger concept with propellant flow path (purple) and the electrical interface are shown (left) [1], and thruster prototype assembly overview (right).

1.2. Concentric Tubular Heat Exchanger Resistojet in Analysis

The Rocket Propulsion Establishment, RPE, Westcott, England, developed the J3 resistojet in 1970s. The thruster was successfully tested at the Oxford University in 1973, obtaining an effective exhaust velocity of 7.57 km/s with an overall thruster efficiency $\eta_{tot} = 68.1\%$, calculated with Eq. (15), a total electric power of 3 051 W and reaching an estimated hot gas temperature in the range 2 500 K. In particular, the heater efficiency was $\eta_h = 97.6\%$, while the main loss was due to the nozzle, with $\eta_n = 69.8\%$ [2]. The design consists of a concentric tubular heat exchanger terminating in a conical nozzle, both made of pure rhenium. A schematic of the thruster is shown in Figure 2. To reduce the heat loss in the radial direction, a vacuum jacket with radiation shields is placed around the concentric tube heat exchanger. In turn, this produces a steep radial temperature gradient, which causes thermal expansion of the heat exchanger its axis. Therefore, a stainless steel bellows is incorporated to manage this expansion. The fabrication technique and assembly procedure of this thruster are described in Ref. [3]. In general, thin walled rhenium tubes are produced by Chemical Vapour Deposition (CVD) and joined by Electron Beam (EB) welding. Compared with the monolithic HTR heat exchanger manufactured by SLM, the J3 thruster assembly was composed of many components, resulting in higher manufacturing lead time and costs, with a structural integrity driven by the EB weld quality of the high number of struts connectors.

Donovan et al. [4] show detailed information on the 3kW experimental hydrogen resistojet. In particular, they provide a full table of measurement and derived data of a test campaign to characterize the thruster. This paper is of great importance for the present work for two main reasons: (1) it gives a set of experimental data with a sufficient thruster design description to set up a validation exercise of a complex multiphysics simulation; (2) it shows a high temperature design conceptually similar to the High Temperature Resistojet. In this paper, a stationary 2D-axisymmetric model of the J3 resistojet is developed using the software COMSOL Multiphysics and the main results are discussed. The experimental data for model validation are gathered from Ref. [4], which provides a set of 14 steady data points with 22 measured quantities, collected over three separate tests for a total of 26 hours of operation. This test campaign was conducted at one-tenth of the design mass flow rate, while experimental data at design point are found in Ref. [2].

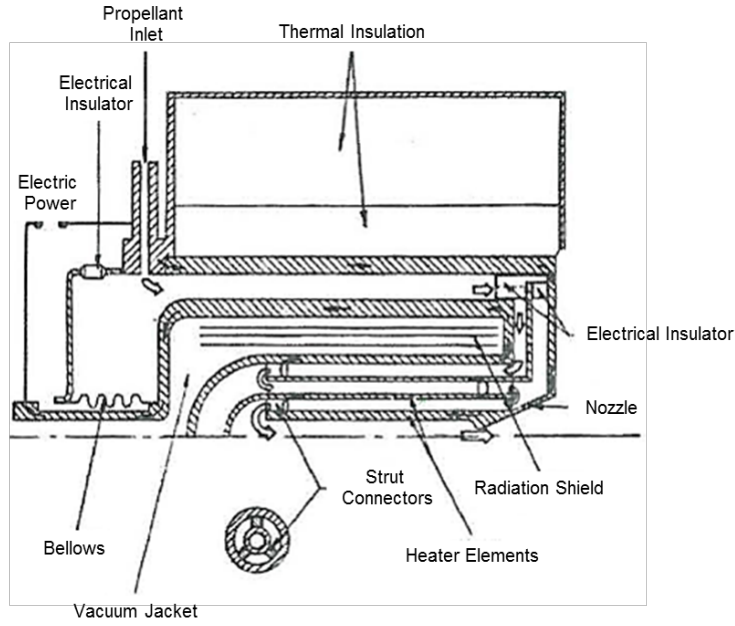


Figure 2: J3 concentric tubular resistojet schematics [5]

2. J3 Nozzle Evaluation

The simplest way of describing a converging-diverging nozzle is by assuming the following: one-dimension and steady problem, ideal gas, Eq. (1), isentropic and compressible flow, Eq. (2) and (3).

$$p = \rho RT \quad (1)$$

$$\frac{T_t}{T} = 1 + \frac{\gamma - 1}{2} M^2 \quad (2)$$

$$\frac{p_t}{p} = \left(\frac{T_t}{T}\right)^{\frac{\gamma}{\gamma-1}} = \left(\frac{\rho_t}{\rho}\right)^\gamma \quad (3)$$

$$\dot{m} = \frac{A^* p_t}{\sqrt{T_t}} \sqrt{\frac{\gamma}{R}} \left(\frac{\gamma + 1}{2}\right)^{-\frac{\gamma+1}{2(\gamma-1)}} \quad (4)$$

where $R = c_p - c_v$ is the gas constant, $\gamma = c_p/c_v$ is the specific heat ratio and M the Mach number. Eq. (4) describes the mass flow rate evaluated at the throat, with section area A^* , where the flow is sonic ($M = 1$). The thermodynamic variables ρ , p and T can be evaluated anywhere along the nozzle longitudinal axis and their respective stagnation values are indicated with a subscript t . However, the assumptions described above are particularly far from the reality when the nozzle Reynolds number is low. In particular, when the nozzle regime is laminar and the reservoir pressure relatively low, the boundary layer, hence the subsonic region on the nozzle throat and diverging section is extensive. It can reach about one third of the nozzle exit radius as described in Ref. [6]. In order to correctly evaluate the nozzle, it is necessary to solve the full N-S equations, which are able to model the strong viscous effect on the nozzle wall. In this section, the problem geometry and boundary conditions necessary for an accurate nozzle modelling are shown step by step, by adding complexity to an initial simple adiabatic nozzle model. The High Mach Number Flow (HMNF) interface is used in COMSOL for the nozzle model and the hydrogen gas thermodynamic properties as function of temperature are found in Ref. [7]. The flow regime is assumed laminar in all cases analyzed.

2.1. Computational grid convergence study

The J3 nozzle has a throat diameter of 1.31 mm, an inlet tube diameter of 2.10 mm, a conical diverging section with a half-angle of 18° and an area ratio of 100. A computational grid convergence test is performed on an adiabatic nozzle with the following inlet conditions: $T_t = 302$ K, $p_t = 10.6$ kPa and an initial Mach number $M_{0,i} = 0.19664$. The nozzle outlet boundary condition is $p_c = 4$ Pa, which is the vacuum chamber pressure. The initial Mach number is evaluated

with Eq.(5) - (7), where w_i is the inlet axial velocity, a_i is the inlet speed of sound evaluated at the inlet, stagnation temperature assumes $T_i = T_t$, A_i is the inlet nozzle area, with $r_i = 1.05$ mm and $\dot{m} = 8.06$ mg/s is the experimental mass flow rate. The inlet density ρ_i is evaluated with Eq. (1) and the hydrogen gas thermodynamic properties ($\gamma(T)$, $\mu(T)$ and $k(T)$) are found in Ref. [7] and implemented in the model.

$$M_{0,i} = w_i/a_i \quad (5)$$

$$a_i = (\gamma RT_i)^{1/2} \quad (6)$$

$$w_i = \dot{m}/(\rho_i A_i) \quad (7)$$

The mass flow rate is calculated at the inlet, throat and exit nozzle sections with Eq. (8), while the thrust is defined with Eq. (9) evaluated at the nozzle exit boundary, with radius R_e , where $p_c = 4$ Pa is the chamber pressure, and w is the axial component of the velocity.

$$\dot{m} = 2\pi \int_0^R (\rho w) r dr \quad (8)$$

$$F = 2\pi \int_0^{R_e} [\rho w^2 + (p - p_c)] r dr \quad (9)$$

A structured computation mesh, is parametrized as function of a refinement parameter f , which is used for the mesh convergence analysis (Figure 3). Both the radial number of elements and the axial number of elements are proportional to f . The radial discretization is divided into two parts (line on the right hand of the nozzle), so that the discretization close to the nozzle wall, i.e. where the boundary layer is located, can be further refined. In particular, the number of radial elements close to the wall is $n_{rw} = 15 \times f$, with an element ratio of 100 (ratio between the first and last radial length) and arithmetic progression. The number of element at the nozzle central part is $n_{rc} = 12 \times f$. The conical diverging section has $n_d = 70 \times f$ with an element ratio of 7 and arithmetic progression. The other boundaries of the nozzle are similarly discretized to obtain the mesh shown in Figure 3.

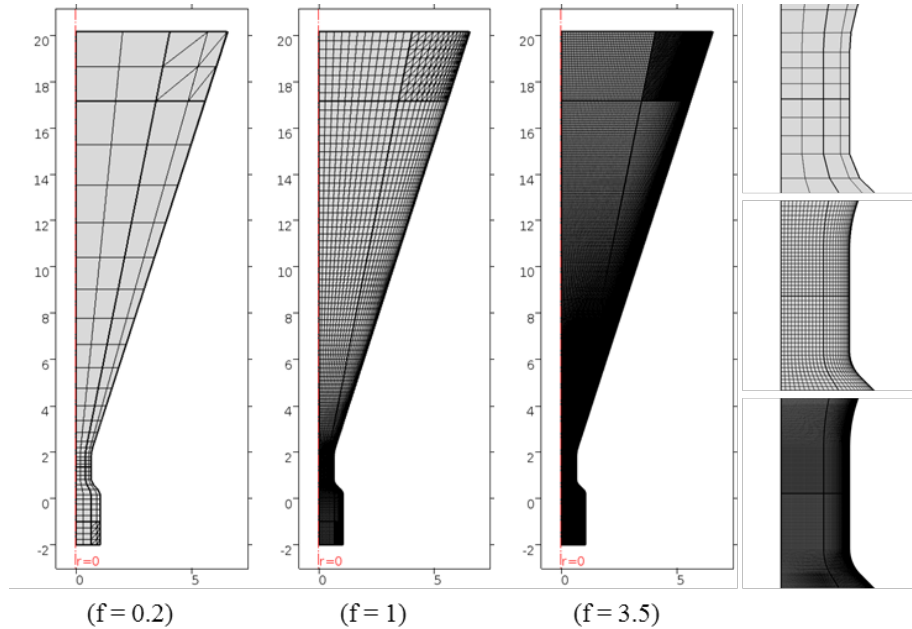


Figure 3: Computational grid of the nozzle geometry as function of the refinement parameter f : nozzle overview (left) and throat detail (right). The total number of elements for these cases is 172, 5 088 and 62 072 respectively.

The relative errors are calculated with respect to the finest mesh solutions ($f = 3.5$). Figure 4 (left) shows the relative errors of mass flow rates calculated at three section of the nozzle: inlet, throat and exit plane. Figure 4 (right) shows

the relative error, evaluated at the nozzle exit plane as an average surface integral, of the variables T , static temperature, p , static pressure, w , axial component of the velocity and u , radial component of the velocity. When the refinement factor is the highest ($f = 3.5$), the average mass flow rate at the three sections is 7.6929 mg/s, while the average values (denoted by an overbar) of the thermodynamic variables calculated at the exit are $\bar{T}_e = 143.26$ K, $\bar{p}_e = 16.940$ Pa, $\bar{w}_e = 1823.7$ m/s and $\bar{u}_e = 266.93$ m/s. When $f = 1$, the average relative error of the mass flow rate at the three nozzle sections is $\bar{\epsilon}(\dot{m}) = -0.24\%$, while at the exit section $\epsilon(\bar{T}_e) = -2.10\%$, $\epsilon(\bar{p}_e) = -2.3\%$, $\epsilon(\bar{w}_e) = -0.02\%$ and $\epsilon(\bar{u}_e) = -1.45\%$. It should be noted that the nozzle stagnation condition, derived in the reference, does not provide the expected mass flow rate of 8.06 mg/s. This is attributable to strong viscous effects, which determine a relatively large boundary layer at the throat region and extended to the nozzle diverging section. As a result, there is a smaller ‘virtual’ throat radius, resulting in a lower mass flow rate.

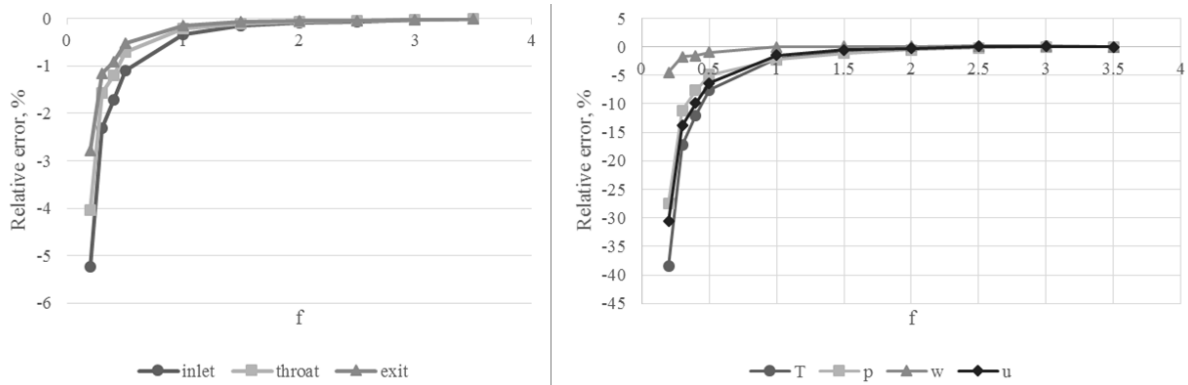


Figure 4: Relative error of mass flow rate (left) and of the average values of T , p , w and u calculated at the nozzle exit (right) as function of the refinement parameter f .

2.2. Parametric sweep of stagnation conditions

The authors in Ref. [4] estimate analytically both the stagnation pressure and temperature at the inlet of the nozzle. These quantities, $T_{t,i}$ and $p_{t,i}$, are taken as initial input for the model stagnation condition, while the initial inlet Mach number is evaluated as described in section 2.1. The outlet boundary condition is the vacuum chamber pressure, p_c , which is a direct measurement. The computational grid parameter f is set to 1.

A first calculation of thrust and mass flow rate is made assuming an adiabatic nozzle (case a). However, the resulting mass flow rate is underestimated by -6% and -9% with respect to the experimental value of 8.06 mg/s from the first to the last test (Figure 5, right). Since the mass flow rate is directly proportional to the stagnation pressure, a correction factor has been extrapolated from the mass flow rate error and applied to the stagnation pressure for each test condition (case b). The resulting mass flow rate error is less than 2% in each case. Finally, a temperature profile is applied to the nozzle wall (case c) assuming that the wall temperature is equal to the stagnation temperature at the inlet and linearly decreases as function of the axial coordinate, z , to the experimental nozzle temperature, T_n . This assumption largely agrees with the solution of the full thruster (discussed in section 3). The described temperature boundary condition is applied through Eq.(10), where $H_{nozzle} = 20.159$ mm.

$$T_w(z) = T_t + (z + 2) \times \frac{(T_n - T_t)}{(H_{nozzle} + 2)} \quad (10)$$

Figure 5 shows the resulting thrust and average mass flow rate respectively, for the three different cases (a – c) described above and compared with the experimental values. The experiments provide accurate thrust and mass flow rate measurements. Here, a mass flow rate is obtained reasonably close to the experimental one, therefore the computational thrust can be used to judge the model accuracy. The calculated thrust is overestimated with a relative error with respect to the experiments between 23% to 29%, from the first to the last test. Figure 6 shows the Reynolds number, defined for a pipe flow in Eq.(11), calculated with the average value of viscosity at the respective sections (inlet, throat and nozzle exit). For a pipe flow, the Reynolds upper limit for a laminar flow is 2100. The exit section exhibits in general the highest Reynolds number because the static temperature rapidly drops along the nozzle diverging section, resulting in a viscosity decrease. As a result, while the flow is guaranteed to remain laminar in a large part of the nozzle, in the diverging section it could be sufficiently high in some cases to determine transition to turbulent.

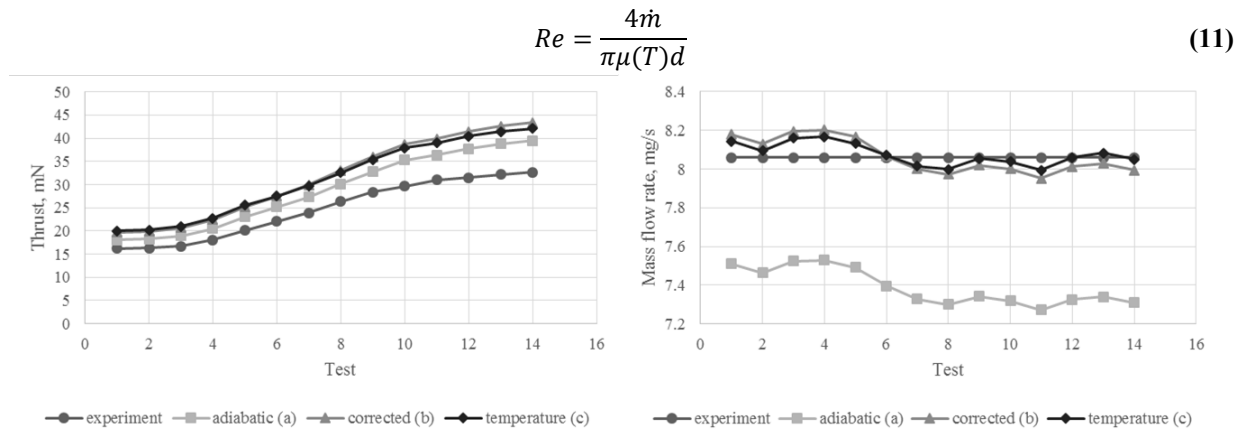


Figure 5: Experimental thrust (left) and mass flow rate (right) compared with simulations results at three different test cases: adiabatic nozzle wall, correction of mass flow rate by changing the stagnation pressure condition and with temperature profile applied to the nozzle wall.

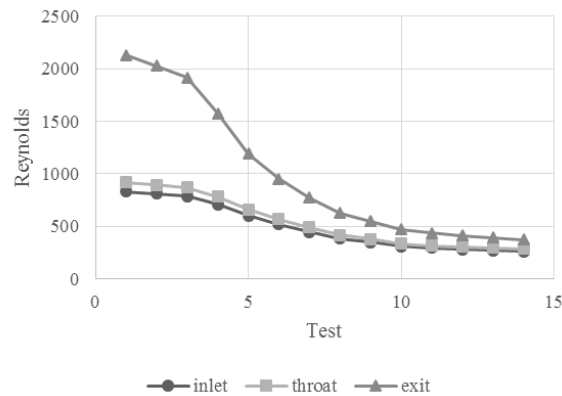


Figure 6: Reynolds number evaluated as at the inlet, throat and exit sections for the 14 experimental points.

2.3. Vacuum chamber effect

In section 2.2, the calculated thrust resulted largely overestimated. In this section, the influence of the vacuum chamber on the thruster performance is investigated. There is no detailed data regarding the vacuum chamber size utilized in the test campaign, however the following is considered a reasonable approximation: length = 1.125 m, radius = 0.5 m, aperture radius = 210 mm. The thruster is positioned at 100 mm from the bottom part of the chamber domain (Figure 7, left). The J3 thruster is here only modelled as a nozzle with its casing contour. The simulation inlet and outlet conditions are set up as already described. However, several cases have been analyzed to highlight the effect of adding particular boundary condition to the problem: Case 1) the vacuum chamber is adiabatic; Case 2) constant temperature (as from experimental measurements) boundary condition applied to the vacuum chamber wall, T_c ; Case 3) temperature boundary condition on the thruster casing top disc, T_{top} , from linear interpolation of the experimental measurements T_n and T_{09} (see Figure 10 for reference), Eq. (12); Case 4) additional vacuum chamber outlet boundary at the back of the thruster, in agreement with the experiment set-up; Case 5) inlet boundary condition determined from the solution of the full thruster (shown in section 3), where the stagnation pressure and temperature and velocity profile are developed.

$$T_{top}(r) = T_n + \frac{r - R_{out}}{R_{th} - R_{out}} \times (T_{09} - T_n) \quad (12)$$

In order to evaluate the thrust, Eq. (9) can be applied to the nozzle without accounting for the chamber pressure, but adding the contribution of the pressure distribution at the top and bottom of the thruster. In all cases, the inlet condition used is the pressure-corrected condition described in the previous section and the resulting mass flow rate remains approximately constant (Table 1). In the unrealistic Case 1 (adiabatic vacuum chamber) the average static temperature in the chamber volume is too high and does not corresponds to reality. By applying $T_c = 293$ K on the chamber wall (Case 2), the thrust evaluation increases by 12%. The effect of adding the top casing temperature profile is minor (Case

3), while in Case 4 the thrust increases of about 4%. Finally, by using temperature and velocity developed profiles from the full thruster model solution as inlet condition (Case 5), the calculated thrust decreases by 1.2%.

Table 1: Effect of different boundary conditions of Cases (1-5) as thrust relative error with respect to the experimental value $F = 32.7$ mN (Test-14).

	Case 1	Case 2	Case 3	Case 4	Case 5
F , mN	-27.76%	-18.97%	-18.21%	-14.82%	-15.88%
\dot{m} , mg/s	8.044	7.994	7.967	8.029	8.042

The calculated pressure on the top disk of the thruster is in general lower than the chamber pressure, contributing negatively to the thrust. In fact, from the standalone nozzle study (section 2.2), where the thrust was overestimated by nearly 30%, this simulation outputs an underestimated thrust between -2.90% to -14.56% from the first to the last test. While the absolute error is reduced, the error direction is changed.

Figure 7 shows the chamber geometry and the Mach number scalar field for Test-1 and Test-14. The latter is characterized by much lower Mach number at the exit, as well as by a larger divergence of the flow at the exit. In particular, the kinetic power lost in radial divergence, Eq.(13), is calculated as 0.97% and 2.01%, of the total kinetic power respectively. The stronger viscous effect in Test-14, determines that the portion of top casing of the thruster with pressure lower than the chamber pressure is wider (Figure 8), leading to a larger negative effect on the calculated thrust.

$$P_{k,r} = 2\pi \int_0^{R_e} \rho w u^2 r dr \quad (13)$$

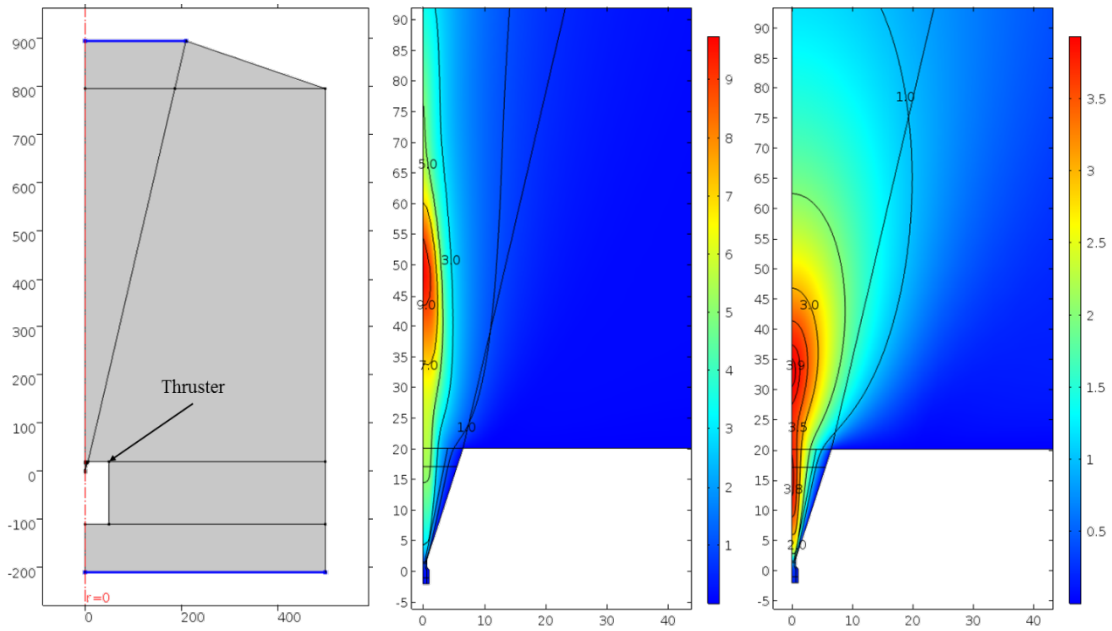


Figure 7: Vacuum chamber geometry with outlet boundaries highlighted (left) and Mach number isocontour near the nozzle: Test-1 (center) and Test-14 (right).

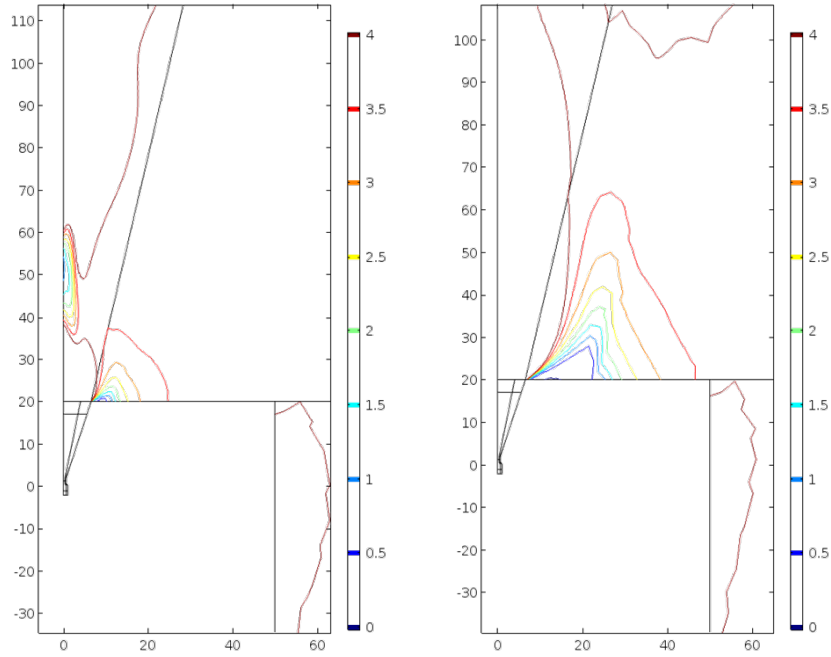


Figure 8: Pressure isocontour for Test-1 (left) and Test-14 (right).

2.4. Error analysis

A quantitative error analysis of the thrust numerical solution due to uncertainty on selected parameters is here shown. Sensitivity analysis is performed using the adjoint method, available within COMSOL, on the fourteen tests in examination. The objective function selected is the thrust, expressed by Eq. (9), while the parameters selected, x_i , are composed by three geometrical terms and six thermodynamic terms. The geometrical parameters are the normal displacement of the inlet, d_i , throat, d_t , and diverging section, d_d , boundaries. Neglecting correlations between these parameters or assuming that these are independent, the error propagation on the thrust is calculated as:

$$\Delta F = \sqrt{\sum_i^n \left(\frac{\partial F}{\partial x_i} \Delta x_i \right)^2} = \sqrt{\sum_i^n (\Delta F_i)^2} \quad (14)$$

where ΔF represents the uncertainty of the computational thrust, and the Δx_i the uncertainty of the selected variables. Since this estimation is based on a linearization of the thrust, it holds for small values of Δx_i . The parameters relative uncertainty $\Delta x_i/x_i$ is kept at 5% for quantities not directly measured in experiments. These are the geometrical displacements and the stagnation condition at the nozzle inlet. The first ones are all set to $\Delta d_i = 42 \mu\text{m}$, which gives a maximum thrust relative uncertainty with respect to geometric variations of 5% among all tests. Whilst the thruster inlet pressure and temperature are directly measured, their values at the nozzle inlet are unknown, therefore their relative uncertainty is set to 5%. For the remaining parameters (T_{09} , T_n , p_c and T_c), the real measurement accuracy available in Ref. [4] is used. The resulting uncertainty of the computed thrust is shown in Figure 9 in the form of error bars. Table 2 shows that calculated partial derivatives of thrust with respect to all parameters selected for the last test, where the calculated thrust uncertainty is $\Delta F_{14} = \pm 2.57 \text{ mN}$. The total thrust uncertainty, $\Delta F/F$, is under 9.5% for all tests.

It has to be noted that the mass flow rate is sensitive to the same list of parameters. In particular, thrust and mass flow rate are proportional, Eq. (4), and observing the sensitivity of the mass flow rate with respect to the same parameters, it can be seen that its relative uncertainty is on the same order of magnitude and with same signs. For this reason, the relative error between computational and measured thrust, also reflects a similar error in mass flow rate. It is evident that the solution is highly sensitive to small geometric variation of the nozzle, and, as expected, to the stagnation condition at the nozzle inlet.

Table 2: List of partial derivatives of thrust with respect to selected variables for the sensitivity analysis (example with Test-14).

	$\frac{\partial F}{\partial d_i}$	$\frac{\partial F}{\partial d_t}$	$\frac{\partial F}{\partial d_d}$	$\frac{\partial F}{\partial T_t}$	$\frac{\partial F}{\partial p_t}$	$\frac{\partial F}{\partial T_{09}}$	$\frac{\partial F}{\partial T_n}$	$\frac{\partial F}{\partial p_c}$	$\frac{\partial F}{\partial T_c}$
Units	N/m	N/m	N/m	N/K	N/Pa	N/K	N/m	N/Pa	N/K
Value	19.386	39.959	2.07	-5.16×10^{-6}	1.25×10^{-6}	-3.07×10^{-6}	1.71×10^{-6}	-7.72×10^{-4}	-2.72×10^{-6}
ΔF_i , mN	1.018	1.309	0.678	-3.95×10^{-1}	1.80	-1.15×10^{-2}	8.41×10^{-3}	-1.00×10^{-2}	-3.98×10^{-2}

2.5. Result and Discussion

The computational thrust diverges from the experiment as the stagnation pressure and temperature increase (from the first to the last test). It is argued that the continuum flow hypothesis loses validity for lower Reynolds numbers, or equally higher Knudsen number. The relative error of the computational thrust with respect to the experiments goes from -2.9% at test 1 to -14.6% in the final test. One possibility is that the no-slip hypothesis on the nozzle diverging section close to the exit is not satisfied, therefore a velocity slip could be present [8]. The effect of a slip flow for a low Reynolds number nozzle is not in itself detrimental, and the resulting skin friction and heat transfer generally decrease, leading to greater expansion [9]. This behavior would agree with the underestimation of thrust for lower Reynolds numbers (Figure 9). Instead of a continuum gas dynamics assumption modelled by full N-S equations, low Reynolds number nozzles could be better modelled by Direct Simulation Monte Carlo (DSMC) in the molecular gas dynamics assumption [10-12]. In conclusion, it is possible that the lower Reynolds number tests solved with N-S have overestimated boundary layer thickness, while DSMC could determine a thinner one and, as a consequence, a higher average Mach number at the exit, hence higher thrust.

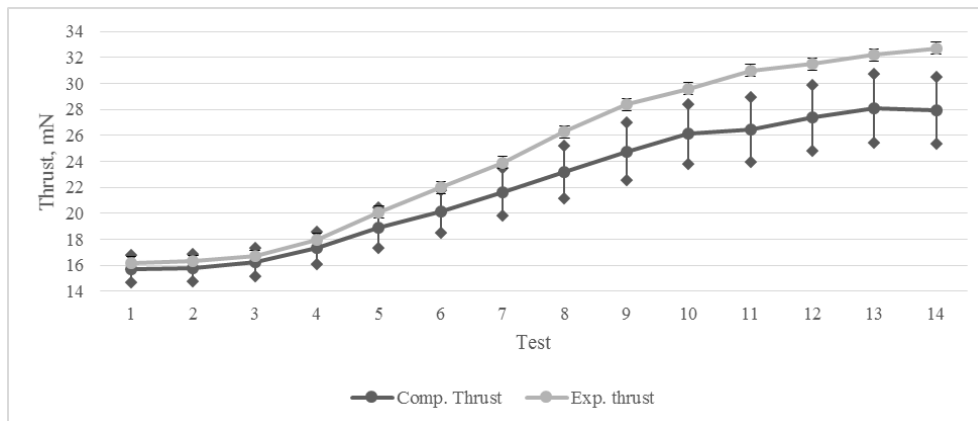


Figure 9: Computed and experimental thrust for the fourteen tests in analysis, with error bars of measurement (from thrust balance measurement accuracy) and model (from sensitivity analysis).

3. Complete J3 thruster model

Whilst the nozzle model can, within the limits discussed above, predict the thrust for a given inlet stagnation condition ($p_{t,n}, T_{t,n}$), the full thruster model could deepen the knowledge of the engine behavior in parts otherwise not accessible for direct measurement. A validation of such model will form the basis for design optimization of the HTR in development (Section 1.1). In section 2 the nozzle has been analyzed showing a possible limit in the assumption of a continuum flow for the lower Reynolds number regimes analyzed. However, the N-S equations are valid within the heat exchanger, where the subsonic flow determines negligible Knudsen numbers. Since the fluidic solution of the nozzle diverging section only depends on its inlet stagnation conditions, a necessary condition for the full thruster model to be valid, is that the stagnation pressure and temperature solution at nozzle inlet are as expected. The full thruster solution can be compared to experiments through a set of available direct measurements (Figure 10), which

include inlet pressure and temperature measured at the propellant inlet tube, $(T_i p_i)$, electric potential and current at the heater terminals, (V, I) , a set of temperatures measured through thermocouples, T_j , and the maximum structural temperature, T_m , measured with an optical pyrometer looking into the nozzle throat.

3.1. Materials and Geometry

The J3 resistojet thruster is modelled here with its main components, including: concentric tubular heat exchanger, nozzle, thermal insulation package, ceramic electric insulators, low emissivity casing and radiation shield composed by thin low-emissivity foils. Fairly complete information on the materials name and grade and geometry for all of the components of the J3 resistojet can be found in Ref. [2-5]. For the modelling, materials are selected from the COMSOL library apart from the fibrous ceramic insulators of the thermal insulation package (Figure 2), such as Dyna-quartz (innermost insulation block) and Min-K2000 (outer insulation block). The thermal conductivity of these fibrous ceramic insulators are found in Ref. [13] and Ref. [14] respectively. The stainless steel surface emissivity of the resistojet case is given as temperature independent ($\varepsilon = 0.08$), while the high temperature electric insulators are made of boron nitride (grade HP), with assumed constant thermal conductivity of $28 \text{ Wm}^{-1}\text{K}^{-1}$.

As described in section 1.2, four heating tubes compose the main heater, while two 2 mm thick tubes form the cold inflow annular flow path of the heat exchanger. The nominal thickness of the four heater tubes from the innermost outwards are: 0.70 mm, 0.165 mm, 0.125 mm and 0.40 mm. It is also known that the struts thickness is 1 mm, the nozzle diverging section thickness is 0.7 mm, the nozzle disk (where the thermocouple T_n is placed) is 1.5 mm thick and the radiation shield foils are 0.025 mm thick. The remaining dimensions have been deduced from a detailed thruster assembly diagram found in [4, 5]. A 2D axisymmetric geometry has been drawn in Solidworks as shown in Figure 10, where the thruster sketch is highlighted and the image used for the reproduction is shown below. The geometry is exported as .DXF and manually optimized for COMSOL computation. The inlet and outlet boundaries and the computational probes utilized to compare the thermocouple measurements are also shown.

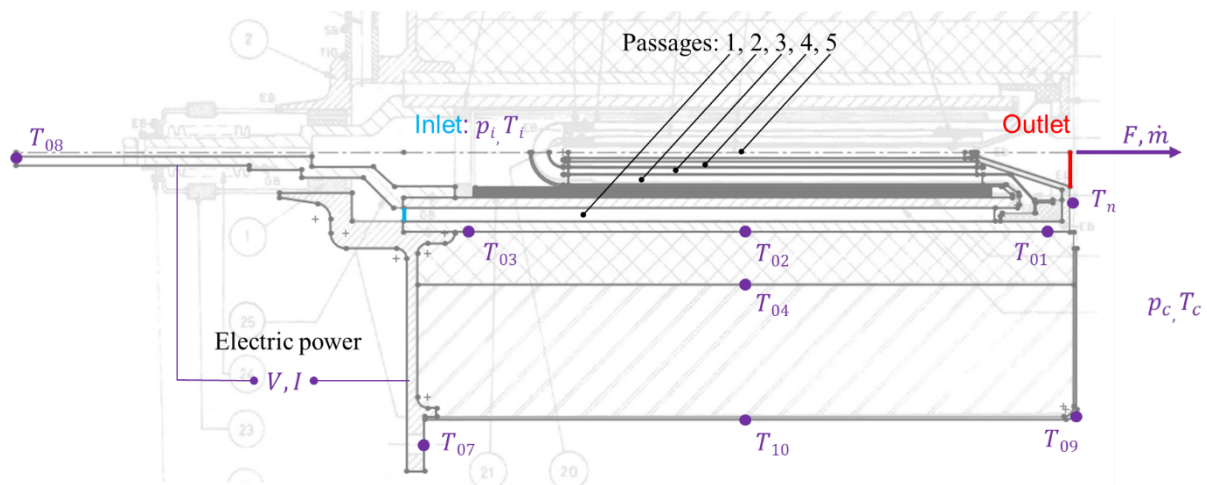


Figure 10: J3 resistojet drawings with direct experimental measurement in purple, inlet and outlet boundary conditions highlighted and numbered concentric tubular heat exchanger annular passages.

3.2. Problem Definitions and Mesh

In the heat exchanger, and more in general for relatively high stagnation pressures, the continuum flow assumption is always valid, so it is the condition of no slip at the heat exchanger surface [9]. The physics interfaces used within COMSOL for the J3 resistojet simulation are HMNF and Electric Current (EC). The first couples the laminar flow interface, applied to compressible flow, with the heat transfer interface. The second one models the Joule heating within the heater elements. The flow is laminar and the inlet stagnation conditions $(p_{t,i}, T_{t,i}$ and $M_{0,i})$ are applied as shown in section 2.1. The outlet boundary condition is imposed on the nozzle exit area, using a hybrid flow (not forcing a supersonic nozzle exit) and setting the static pressure of the vacuum chamber, p_c , in the same way of the single nozzle study. Surface-to-surface radiation is applied on the internal wall boundaries of the whole heat exchanger and nozzle. For the approximation of the form factors, the hemicube method is used with default values. The surface-to-ambient radiation boundaries include the thruster back plate surface and the stainless steel low-emissivity case.

The EC interface is coupled in temperature with the HMNF. The rhenium electrical conductivity is given as a polynomial function of the temperature in the material library. As an initial value, the heat exchanger is at 0 V potential. Because there is only one dependent variable in EC (the potential V), it is sufficient to apply the experimental terminal

current I as boundary condition on the four concentric resistive elements independently. The mesh is tailored by refining the flow channels with a structured mesh, while a free triangular mesh is used for the solid domains. The nozzle is meshed as in the section 2.1, as shown in Figure 11 (left). A computational grid convergence study has not been conducted in this case. Nonetheless, a relatively coarse mesh has been used to investigate on the nonlinear behavior of this multiphysics simulation and the results are accurate in the measure that the mass flow rate is conserved within 1% between the inlet and the outlet boundaries.

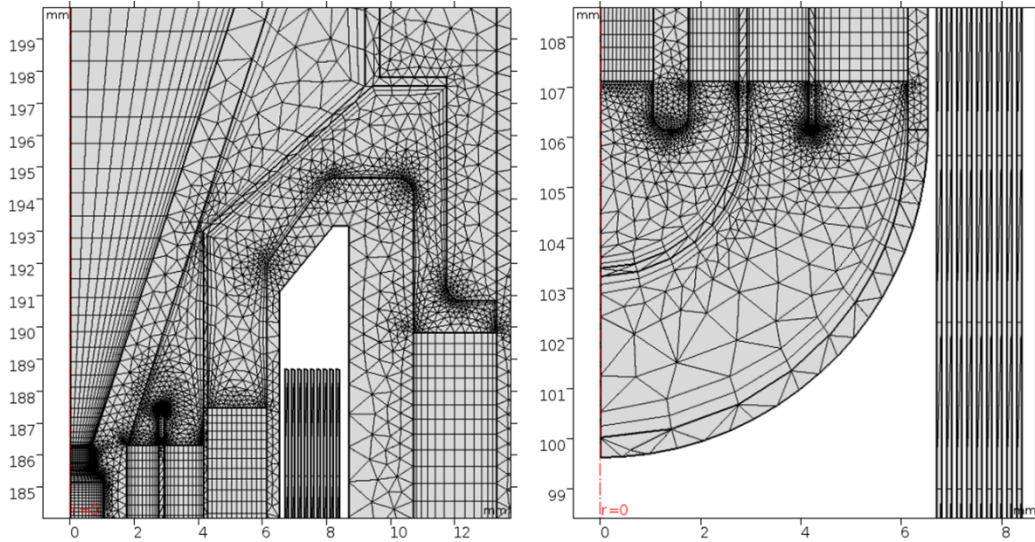


Figure 11: Computational grid of J3 thruster: nozzle region (left) and elbow region (right) (axis units in mm).

3.3. Results and Discussion

In this section, the multiphysics simulation results on the Test-14 conditions and at the thruster design point are shown and discussed. Table 3 shows the relative error of the multiphysics solution with respect to the experimental direct measurements and to the expected stagnation condition at the nozzle inlet, $p_{t,n}$ and $T_{t,n}$. The electrical current is a model input, and its value has been chosen by trial and error to obtain a small relative error of the mass flow rate. The thermocouple computational probes show a good agreement all over the engine, with greater underestimation of the temperatures at the nozzle top disk, T_n , and at the inlet of the thruster, $T_{01} - T_{03}$. The former could derive by an overall underestimation of the temperature at the nozzle inlet, $T_{t,n}$, while the latter could be due to the geometric simplification at the bottom of the thruster. Figure 12 shows the solution of the multiphysics problem as electric potential of the heater in V (left) and the temperature distribution in K for both the fluid and solid domains (right). Table 4 shows the relative errors of the multiphysics solution of the thruster at its design point as compared with experimental data available in Ref. [2], where thermocouple measurements are not provided. In this case, the computational electric current is taken equal to experimental one.

Table 3: Relative error of the solution with respect to experimental values of Test-14.

I	V	P_e	$T_{t,n}$	$p_{t,n}$	\dot{m}	T_m	T_n
-7.00%	1.21%	-5.88%	-5.86%	-1.74%	-1.77%	-0.88%	-22.13%
T_{01}	T_{02}	T_{03}	T_{04}	T_{07}	T_{08}	T_{09}	T_{10}
-6.68%	-16.56%	-27.50%	-0.39%	-3.22%	3.91%	-8.57%	0.94%

Table 4: Relative error of the solution with respect to experimental values at design point ($I = 208$ A).

V	P_e	R	$T_{t,n}$	$p_{t,n}$	\dot{m}	T_m
9.05%	9.29%	9.32%	3.2%	0.77%	-9.64%	-0.6%

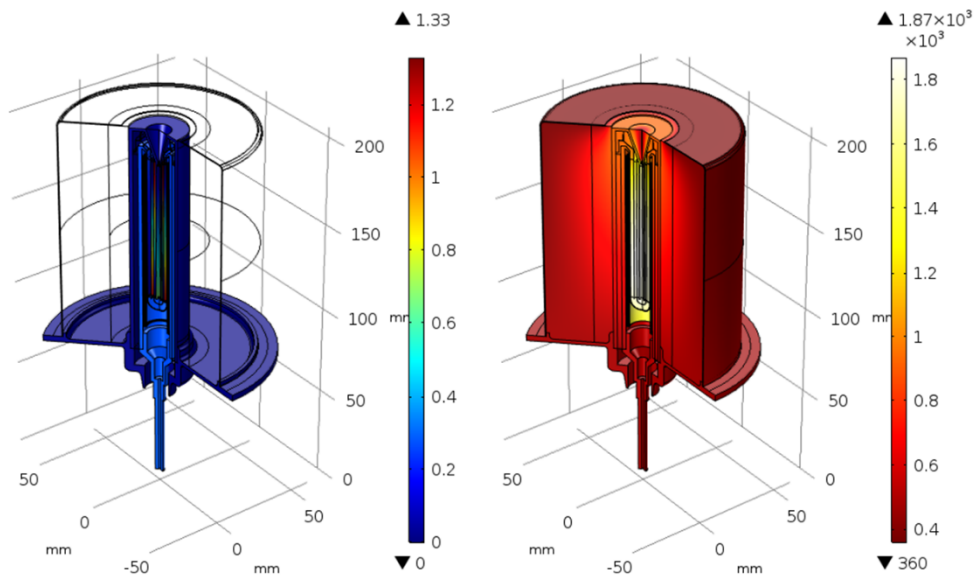


Figure 12: Simulation results on Test-14: heater electric potential in V (left) and thermal solution in K (right) (axis units in mm).

The total thruster efficiency can be calculated using Eq.(15), where for Test-14 $P_k = \dot{m}w^2/2 = 78.1$ W is the axial kinetic power of the jet, $P_e = 181.7$ W is the total electric power as sum of the voltage-current products of the four heater tubes and $P_{i,p} = 43.3$ W is the propellant inlet power. When the electric power is zero, this equation can also be used to calculate the efficiency in cold gas mode.

$$\eta_{tot} = \frac{P_k}{(P_e + P_{i,p})} = \frac{g_0 F I_{sp}}{2(\sum VI + c_p T_i)} \quad (15)$$

The current simulation determines a total thruster efficiency of 29.8%, taking into consideration the axial kinetic power evaluated with the single nozzle study (Section 2), where the vacuum chamber influence on the thruster body is taken into account. The total efficiency can also be broken down into two parts, the nozzle efficiency, $\eta_n = P_k/P_{0,n}$, and the heat exchanger efficiency, $\eta_h = P_{t,n}/(P_e + P_{i,p})$, where the simulation provides $P_{t,n} = \dot{m}h_{t,n} = 199.2$ W, for resulting efficiencies of $\eta_n = 39.2\%$ and $\eta_h = 88.5\%$ and pressure drop $p_d = p_i - p_{t,n} = 14.552$ kPa.

Figure 13 shows the temperature distribution evaluated at the centerline of the concentric tubular heat exchanger passages up to the nozzle exit, where the static temperature drops (passage 5). The graph highlights the not-ideal behavior of the J3 heat exchanger, which rather should rise the temperature of the propellant monotonically, so that the energy is stored as more internally as possible and thermal losses are reduced to a minimum. Instead, in the Test-14 analyzed the maximum temperature is achieved already after the first recirculation (passage 2), whilst it decreases at the following one (passage 3) to increase again at the next one (passage 4). As Figure 12 shows, the heat exchanger develops a higher temperature at the back end of the thruster, where $T_m = 1870$ K for Test-14. The temperature distribution at the design mass flow rate shows a better functionality of the J3 engine, however still with a temperature decay in channel 3.

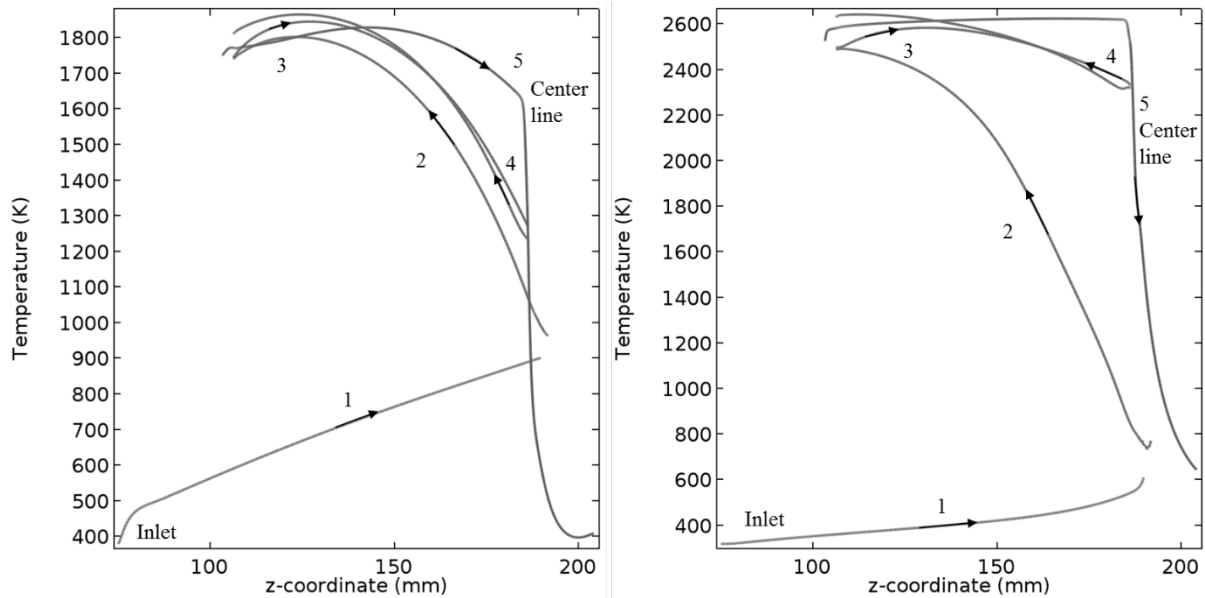


Figure 13: Temperature distribution at the center lines of the heat exchanger passages (numbered): Test-14 (left) and J3 at design point (right).

The full thruster simulation here shown agrees fairly well globally. Nevertheless, some temperature probes suggest that either some physical or geometrical assumptions must be reevaluated for better agreement. It has to be noted that the problem of non-linearity makes the solution very sensitive to the geometry. As an example, the mass flow rate is determined by the stagnation enthalpy at the inlet of the nozzle, Eq. (4), which stems from the pressure drop across the heat exchanger. The pressure drop depends on the hydraulic diameters of the heat exchanger annular channels and the local electric power dissipation of the heater tubes depends on their section area. Unfortunately, the annular gaps between the tubular elements are unknown. Future work within the J3 thruster study could include a global parametrization of the thruster geometry within certain tolerances to investigate on a broader sensitivity analysis. The results on the J3 thruster also indicates that the concentric tubular heat exchanger design could be optimized in terms of power dissipation. In particular, the heater tubes thickness could vary along the flow path to enable heat transfer optimization.

Conclusions

The paper shows multiphysics modelling of the J3 resistojets with concentric tubular heat exchanger, which uses hydrogen gas as propellant. The study has been divided into two parts: isolated nozzle with analysis of the vacuum chamber effect on the performance (section 1) and full thruster multiphysics simulation to deepen the knowledge of this particular resistojets design (section 2). It is shown that the continuum flow assumption is not valid at the nozzle diverging section where a slip velocity could be present. DSMC could be adopted to obtain a better agreement in the lower Reynolds number test cases.

It has been noted that the significant non-linearity of the full thruster problem determines a very sensitive solution to geometric and material properties assumptions. However, the model results show fairly good agreement with experiments and the current study highlights where and how the model could be improved. The application of the model to the High Temperature Resistojets in development at the University of Southampton is thought to be encouraging for future validation and design optimization. The HTR will be tested at the University of Southampton and experimental results will be used as input for a multiphysics simulation study of the same type as demonstrated here for the J3 thruster.

Acknowledgments

This work has been supported by the Doctoral Training Partnership through the Engineering and Physical Sciences Research Council (EPSRC) [grant number EP/M50662X/1].

References

- [1] Romei, F., A. Grubišić, and D. Gibbon, *Manufacturing of a high-temperature resistojets heat exchanger by selective laser melting*. Acta Astronautica, 2017.

- [2] Donovan, J. and W. Lord, *Performance Testing of a 3kW Hydrogen Resistojet*. 1973, DTIC Document.
- [3] Sherwood, P., *Construction of a High Performance Resistojet for Satellite Propulsion*. 1978, DTIC Document.
- [4] Donovan, J.A., W.T. Lord, and P.J. Sherwood, *Fabrication and Preliminary Testing of a 3kW Hydrogen Resistojet*, in *The AIAA 9th Electric Propulsion Conference*. 1972.
- [5] Page, R.J. and R.A. Short, *Design of High-Performance Resistojets for Advanced Spacecraft*, in *9th Aerospace Sciences Meeting-Separate Papers - AIAA*, A.R. Technology, Editor. 1971. p. No.71-195.
- [6] Romei, F., et al., *A Thermo-Fluidic Model for a Low Power Xenon Resistojet*, in *International Electric Propulsion Conference*. 2015: Hyogo-Kobe, Japan.
- [7] McCarty, R.D., J. Hord, and H. Roder, *Selected properties of hydrogen (engineering design data)*. 1981, National Engineering Lab.(NBS), Boulder, CO (USA).
- [8] Kim, S.C., *Calculations of Low-Reynolds-Number Resistojet Nozzles*. *Journal of Spacecraft and Rockets*, 1994. **31**(2): p. 259-264.
- [9] Edwards, I., *A theoretical study of the performance of resistojet nozzles*. 1972, University of Southampton.
- [10] Chung, C.-H., et al., *Low-density nozzle flow by the direct simulation Monte Carlo and continuum methods*. *Journal of Propulsion and Power*, 1995. **11**(1): p. 64-70.
- [11] Alexeenko, A.A., et al., *Numerical modeling of axisymmetric and three-dimensional flows in microelectromechanical systems nozzles*. *AIAA journal*, 2002. **40**(5): p. 897-904.
- [12] Ketsdever, A.D., et al., *Experimental and numerical determination of micropropulsion device efficiencies at low reynolds numbers*. *AIAA Journal*, 2005. **43**(3): p. 633-641.
- [13] Rolinski, E.J. and T.L. Sweeney, *Thermal conductivity of fibrous silica*. *Journal of Chemical & Engineering Data*, 1968. **13**(2): p. 203-206.
- [14] MatWeb, *Thermal Ceramics Min-K 2000 Data Recorder Molded Min-K Insulation*. <http://www.matweb.com>, 2017.